Integration of optical clearing and optical sectioning microscopy for three-dimensional imaging of natural biomaterial scaffolds in thin sections

S-ja Tseng*
Ying-Hui Lee*
Zhi-Hao Chen
National Tsing Hua University
Department of Chemical Engineering
101 Section 2 Kuang Fu Road
Hsinchu 30013
Taiwan

Hui-Hao Lin
Chih-Yung Lin
National Tsing Hua University
Institute of Biotechnology and Brain Research Center
101 Section 2 Kuang Fu Road
Hsinchu 30013
Taiwan

Shiue-Cheng Tang
National Tsing Hua University
Department of Chemical Engineering
101 Section 2 Kuang Fu Road
Hsinchu 30013
Taiwan
E-mail: sctang@che.nthu.edu.tw

Abstract. The intrinsic turbidity of scaffolds formed by natural biomaterials such as collagen fibers prevents high-resolution light microscopy in depth. In this research, we have developed a new method of using light microscopy for penetrative three-dimensional (3-D) visualization of scaffolds formed by collagen, chitosan, or cellulose. First, we applied an optical-clearing solution, FocusClear, to permeate and reduce the turbidity of the scaffolds. The improved photon penetration allowed fluorophores for efficient excitation and emission in the FocusClear solution. Confocal microscopy was applied to achieve cellular-level resolution up to 350 μm for both the fibroblast/collagen and the osteoblast/chitosan constructs and micrometer-level resolution up to 40 μm for the cellulose membrane. The depth of imaging of the cellulose membrane was further improved to 80 μm using two-photon microscopy. Significantly, these voxel-based confocal/two-photon micrographs allowed postrecording image processing via Amira projection algorithms for 3-D visualization and analysis of the scanned region. Although this optical method remains limited in viewing block scaffolds in thin sections, our approach provides a noninvasive way to microscopically examine the scaffold structure, which would be a valuable tool to studying biomaterials and their interactions with the molecule/cell of interest within the scaffold in an integrated fashion.
[DOI: 10.1117/1.3158998]

Keywords: confocal microscopy; collagen; chitosan; cellulose; three-dimensional (3-D) microscopy.

Paper 08440R received Dec. 16, 2008; revised manuscript received Apr. 22, 2009; accepted for publication May 15, 2009; published online Jul. 10, 2009.

1 Introduction

Natural biomaterial scaffolds formed by proteins (such as collagens), chitosan, or cellulose have been widely used in tissue-engineering applications for injury repair and wound healing to facilitate the regeneration processes.[1–3] In addition, matrices of collagen, chitosan, and cellulose can be engineered to a broad range of chemical and mechanical properties as well as a variety of forms and shapes for three-dimensional (3-D) scaffold design.[4–6] To date, electron microscopy and light microscopy are the standard tools to study the surface and sections of the biomaterial scaffold. However, because the standard two-dimensional (2-D) analysis confines visualization of the architecture at a specific cut plane, 3-D representation of image data over an area of interest is preferable for *in situ* visualization and assessment of the scaffold and its interaction with the molecule/cell of interest.

Among the available imaging technologies, optical sectioning microscopy such as confocal microscopy generates a sharp 2-D image at the plane of focus; incrementing the plane of focus creates a series of optical sections at different depths in the specimen, which allows for construction of a 3-D image.[7] When a tissue specimen is sufficiently transparent so that light can pass through with minimal scattering (such as the Zebrafish embryo[8]), optical sectioning microscopy provides a useful tool to study the 3-D configuration of molecules of interest in the sample. Unfortunately, scaffolds formed by collagen, chitosan, or cellulose are typically nontransparent, which seriously limits their optical accessibility for confocal microscopy or light microscopy in general.

Recent progress in optical clearing provides a useful means to enhance photon penetration into turbid tissues such as skin for optical examination.[9–16] This approach, for example, leads to improved signal detection in optical coherence tomography (OCT),[9] Fourier transform infrared spectroscopic imaging,[10] Raman spectroscopy,[17] and second-harmonic generation (SHG) imaging.[18] Optical clearing also facilitates 3-D organ imaging using optical transmission and emission

*Both authors contributed equally to this work.
Address all correspondence to: Shiue-Cheng Tang, Department of Chemical Engineering, National Tsing Hua University, Hsinchu 30013, Taiwan. Tel: +886-3-571-5131, ext. 33649; Fax: +886-3-571-5408; E-mail addresses: sctang@che.nthu.edu.tw

1083-3668/2009/14(4)/044004/9/$25.00 © 2009 SPIE

tomography.[19–21] Nonetheless, the integration of optical clearing with high-resolution (μm-level) microscopy for in-depth tissue imaging remains a field under development.

Previously, a set of bioimaging technologies in sample preparation, confocal microscopy, and postrecording image processing was developed for visualization of neural circuits in the brain of fruitfly *Drosophila melanogaster* ($\sim$130 μm in thickness) at the subcellular level without employing tissue dehydration, embedding, and sectioning.[22–24] In the present study, we extend the developed technologies for penetrative 3-D imaging of natural biomaterial scaffolds. We appreciate that the intrinsic opacity of the scaffold matrices can prevent efficient light penetration and signal detection for high-resolution imaging of the scaffolds formed by collagen, chitosan, or cellulose. We therefore applied an optical-clearing solution (FocusClear, with a refractive index at 1.46, U.S. Patent 6,472,216-B1) to permeate and reduce the opacity of the scaffold to improve photon penetration during microscopy.[25]

In this research, we show that the improved photon penetration led to a clear visualization of the proliferation/infiltration of fluorescent-labeled fibroblasts and osteoblasts into the collagen and chitosan scaffolds, respectively. Results using optical sectioning microscopy to combine with optical clearing for in-depth visualization of the collagen and chitosan tissue-engineering constructs and cellulose membranes are presented and discussed in this report.

2 Materials and Methods

2.1 *Natural Biomaterial Scaffolds*

The collagen scaffolds were purchased from BD Biosciences (Bedford, Massachusetts); Cat. No. 354613, BD 3-D collagen composite scaffold). The scaffold consists of type I and III collagens derived from bovine hide with a cylinder shape and a dimension of $\sim$5 mm (diameter) $\times$ 3 mm (height). The chitosan scaffolds were prepared by following the protocol published previously.[26] Briefly, chitosan powders with a molecular weight at $\sim$400 K (Koyo Chemical Co., Ltd., Japan) were dissolved in 1% acetic acid to make a 1% chitosan solution. The solution was then frozen in a 60-mm Petri dish and lyophilized to form a sheet of porous scaffold. Scaffolds with a dimension of $\sim$5.5 mm (diameter) $\times$ 1.5 mm (height) were cut from the sheet and transferred to a 48-well plate. The microporous membrane of cellulose scaffold was a gift from Sartorius AG (Göttingen, Germany).[27] The membrane was approximately 250 μm in thickness and was cut into squares of 1 cm $\times$ 1 cm prior to imaging. In conventional bright-light microscopy (Fig. 1), scaffolds were immersed in phosphate-buffered saline (PBS, Sigma, St. Louis, Missouri) or FocusClear solution (CelExplorer, Hsinchu, Taiwan) overnight prior to being imaged by a Nikon TS100 inverted microscope (Tokyo, Japan) to compare their light penetration.

2.2 *Cell Culture and Preparation of the Fibroblast/Collagen and Osteoblast/Chitosan Constructs*

Humane HT-1080 fibroblasts (ATCC, Manassas, Virginia) were stably transfected with a vector carrying an expression cassette of enhanced green fluorescent protein (EGFP) as previously described.[28] The same protocol was used to generate a stable line of human Saos-2 osteoblasts (ATCC) carrying an expression cassette of Ds-Red (Clontech, Mountain View, California). Both stable lines of fibroblasts and osteoblasts were grown in Dulbecco's modified Eagle's medium (DMEM) supplemented with 10% fetal bovine serum, 100 U/mL penicillin, 100 μg/mL streptomycin, and 0.25 μg/mL puromycin (selection pressure) at 37 °C in a humidified atmosphere of 5% CO_2. The EGFP-labeled HT-1080 fibroblasts (1×10^6) were seeded onto the collagen scaffold, and the Ds-Red-labeled Saos-2 osteoblasts (1.5×10^6) were seeded onto the chitosan scaffold. Seeding was carried out in the wells of a 96-well plate. One day after the seeding, both the fibroblast/collagen and the osteoblast/chitosan constructs were transferred to the wells of a 24-well plate for a 7-day cell culture to allow cellular proliferation and infiltration into the scaffold.

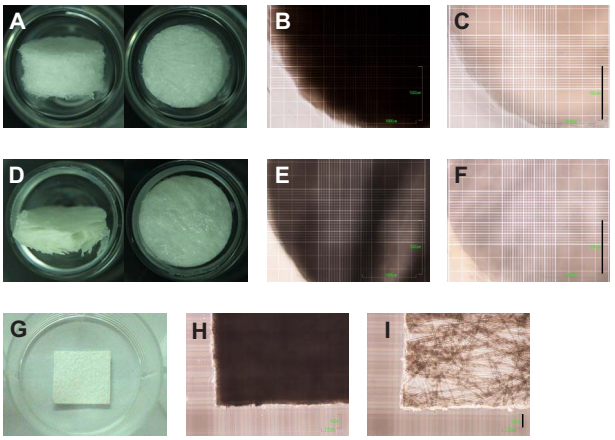

Fig. 1 Optical clearing of collagen, chitosan, and cellulose scaffolds. (a) The gross image of the collagen scaffold with a diameter $\sim$5 mm and height $\sim$3 mm (left: side view; right: top view). The scaffold was immersed in saline (b) or FocusClear solution (c) prior to being imaged by a standard inverted microscope (Nikon TS100) from the top of the scaffold aiming at the bottom-left corner. Scale bar=1 mm. (d) The gross image of the chitosan scaffold with a diameter $\sim$5.5 mm and height $\sim$1.5 mm (left: side view; right: top view). The scaffold was immersed in saline (e) or FocusClear solution (f) prior to imaging. Scale bar=1 mm. (g) The gross image of the microporous cellulose membrane (cut into 1 cm $\times$ 1 cm with a thickness of 250 μm). The membrane was immersed in saline (h) or FocusClear solution (i), which reveals the polyester reinforcement fibers in the membrane after the cellulose matrix became transparent. Scale bar=100 μm. In (b), (c), (e), and (f), the focal plane was on the background, the grid surface of a hemacytometer. In (h) and (i), the focal plane was on the cellulose membrane.

2.3 *Quantification of the Optical-Clearing Effect*

The heat-induced gel formation of bovine serum albumin (BSA; Sigma)[29,30] in the wells of a 96-well plate was used to quantify the optical clearing effect of different reagents. 50 μl of BSA in PBS (350 mg/ml) was transferred to one well of a 96-well plate. Afterward, the plate was carefully sealed and placed in a water bath at 60 °C for 2 h to induce the formation of a layer of BSA protein gel at the bottom of each well. 100 μl of different reagents including FocusClear, dimethyl sulfoxide (DMSO, Sigma), glycerol (Sigma), and PBS (negative control) were placed on top of the BSA gel for optical

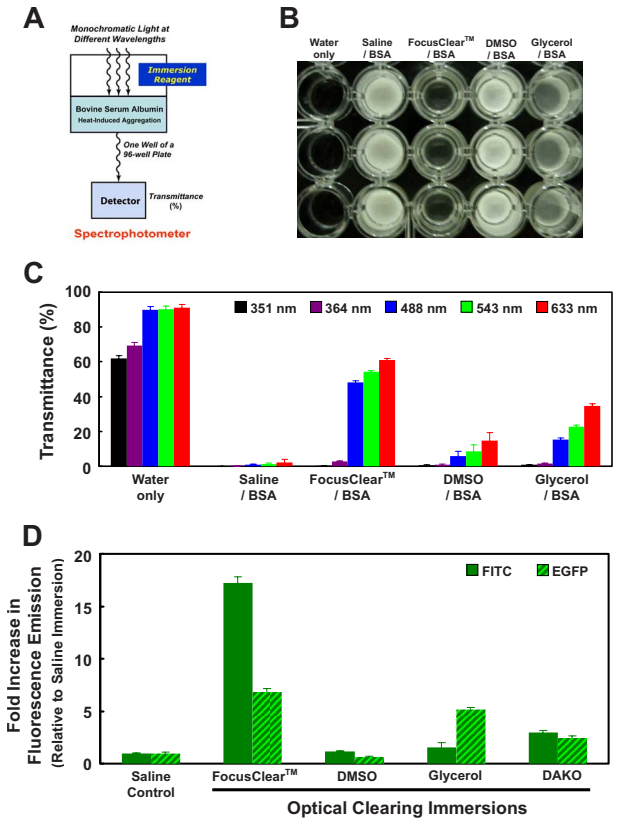

Fig. 2 (a) A schematic diagram of using a layer of light-scattering BSA aggregates and spectrophotometry to quantify the optical-clearing effect. (b) A gross image of a part of a 96-well plate with BSA layers immersed in saline, FocusClear, DMSO, or glycerol. Positive control: wells in water (without the BSA layer; far left). (c) Quantification of the optical-clearing effect. The percent transmittance of (b) was measured at 351, 364, 488, 543, and 633 nm via a microplate reader. Results are presented as mean±standard deviation (n=6). (d) The effect of optical clearing on the increase in fluorescence emission from the FITC- or EGFP-doped BSA layer. Confocal microscopy was used to perform fluorescence excitation/emission 200-μm deep into the BSA layer. A laser line at 488 nm was used for excitation. A long-pass 505-nm filter was used to collect the fluorescence emission. Results are presented as mean±standard deviation (n=6).

clearing for 2 h. Afterward, the percent transmittance of light at 351, 364, 488, 543, and 633 nm was measured via a microplate reader (SpectraMax M2e, Molecular Devices, Sunnyvale, California). Wells with 150 μl of water were used as the positive control. A schematic diagram of the setup is shown in Fig. 2(a).

We used confocal microscopy (LSM 510, Carl Zeiss, Jena, Germany) to evaluate the impact of optical clearing on fluorescence detection. Prior to initiating the heat-induced gel formation of BSA, fluorescein isothiocyanate (FITC, 10 μg/ml, Sigma), or EGFP (10 μg/ml, BioVision, Mountain View, California) was dissolved in the BSA/PBS solution. After gel formation (in a BD Falcon 96-well imaging plate) and the subsequent optical clearing by FocusClear, DMSO, glycerol, DAKO aqueous mounting medium (Carpinteria, California), or PBS (negative control), confocal microscopy employing a 488-nm argon laser and a Fluar 20× objective (Carl Zeiss, NA=0.75) was used to excite FITC and EGFP 200 μm under the gel surface. The fluorescence emission was collected using a long-pass 505-nm filter. The "line" scanning pattern was used and the scanning speed=8. The pixel intensity, ranging from 0 to 255, was set to be the mean value of four scans. The detection gain was carefully adjusted to avoid signal saturation. The *Histogram* function of the LSM 510 software (version 3.2, Carl Zeiss) was used to obtain the frequency distribution of pixels at different intensities, which subsequently was used to calculate the total intensity from the scanned area of 1024×1024 pixels (0.41×0.41 μm^2).

2.4 *Sample Preparation for Imaging*

The blank collagen and chitosan scaffolds were directly immersed in the FocusClear solution overnight prior to being imaged via confocal microscopy. The autofluorescence of collagen and chitosan induced by the 488-nm laser was used to examine their scaffold structures.[31,32] The EGFP-fibroblast/collagen and Ds-Red-osteoblast/chitosan constructs were fixed with 4% paraformaldehyde for 40 min and permeabilized with 2% Triton X-100 for 2 h in PBS at room temperature. Prior to FocusClear immersion, samples of the EGFP-fibroblast/collagen constructs were stained with propidium iodide (PI, 62.5 μg/ml, Molecular Probes, Eugene, Oregon) overnight to label the nuclei. Samples of Ds-Red-osteoblast/chitosan constructs were directly immersed in the FocusClear solution without additional labeling. The microporous cellulose matrix, on the other hand, was stained with Calcofluor White M2R (Sigma) in PBS (5 mg/ml) for 20 min,[33] rinsed in blank PBS, and followed by FocusClear immersion prior to confocal/two-photon microscopy.

2.5 *Imaging Settings*

Confocal imaging of the FocusClear-immersed scaffolds/constructs was performed with a Zeiss LSM 510 confocal microscope (Carl Zeiss). For imaging the blank collagen and chitosan scaffolds, a 488-nm argon laser was used to induce the autofluorescence; a long-pass 505-nm filter was used to collect signals. The PI-stained EGFP-fibroblast/collagen constructs were excited at 543 nm (PI excitation, a helium/neon laser) and 488 nm (EGFP excitation). A long-pass 560-nm filter and a band-pass 505- to 530-nm filter were used to collect signals from PI and EGFP, respectively. The Ds-Red-osteoblast/chitosan construct was excited at 543 nm (Ds-Red excitation) and 488 nm (to induce autofluorescence from chitosan). Band-pass filters of 560 to 615 nm and 505 to 530 nm were used to collect signals from Ds-Red and chitosan, respectively.

The Calcofluor-labeled cellulose matrix was excited at 364 nm with a UV laser, and the fluorescence emission was detected by a 385-nm long-pass filter in confocal microscopy. In two-photon microscopy (performed by a Zeiss LSM510 META microscope), the labeled cellulose membrane was excited by an infrared laser at 820 nm (Chameleon-XR ultrafast Ti-Sapphire laser, Coherent, Inc., Santa Clara, California), and the fluorescence emission was detected by a band-pass 390- to 465-nm filter.

A long-distance C-Apochromat 40× water immersion objective (Carl Zeiss, NA=1.1) was used to acquire the images in Figs. 3, 4(a), and 4(b). A C-Apochromat 40× water immersion objective (Carl Zeiss, NA=1.2) was used to acquire the

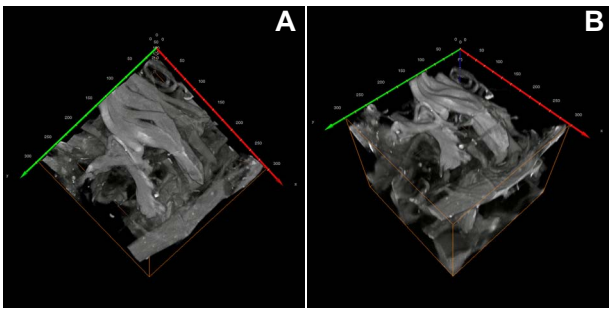

Fig. 3 Three-dimensional imaging of the collagen scaffold. Stereo projection of the scaffold image stack creates a 3-D visualization of the imaged region. (a): top view; (b): side view. A 360-deg panoramic presentation of the scanned region is shown in Video 1. Dimensions of the scanned volume: 290 μm (x)$\times$290 μm (y)$\times$250 μm (z, depth).

images in Figs. 5 and 6. A Fluar 10$\times$ objective (Carl Zeiss, NA=0.5) was used to acquire the images in Figs. 4(c), 4(d), and 7. The voxel size (x μm$\times y$ μm$\times z$ μm) was set at (0.29$\times$0.29$\times$2.5), (0.41$\times$0.41$\times$3.5), (0.29$\times$0.29$\times$2), (0.82$\times$0.82$\times$4), (0.07$\times$0.07$\times$1), (0.06$\times$0.06$\times$1), and (0.06$\times$0.06$\times$0.5) for Figs. 3, 4(a)–4(d), 5(a)–5(h), 6, and 7, respectively. Each confocal/two-photon micrograph consists of 1024$\times$1024 pixels at the x/y plane. The number of optical slices along the z axis was at 101, 101, 151, 89, 41, 81, and 85 for Figs. 3, 4(a)–4(d), 5(a)–5(h), 6, and 7, respectively. The "line" scanning pattern was used in each confocal/two-photon microscopy and the scanning speed=8. The pixel intensity, ranging from 0 to 255, was set to be the mean value of four scans for confocal microscopy and two scans for two-photon microscopy.

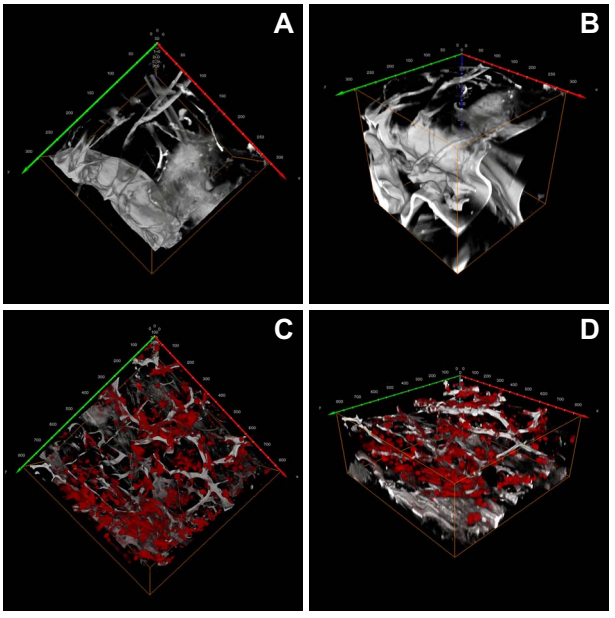

Fig. 4 Three-dimensional imaging of the chitosan scaffold and osteoblast/chitosan construct. (a) and (b) Stereo projection of the scaffold image stack creates a 3-D visualization of the imaged region. (a) top view; (b) side view. Dimensions of the scanned volume: 290 μm (x)$\times$290 μm (y)$\times$300 μm (z, depth). (c) and (d) Stereo projection of the osteoblast/chitosan image stack. Human Saos-2 osteoblasts were labeled with Ds-Red. (c): top view; (d): side view. A 360-deg panoramic presentation of (d) is shown in Video 3. Dimensions of the scanned volume: 842 μm (x)$\times$842 μm (y)$\times$352 μm (z, depth).

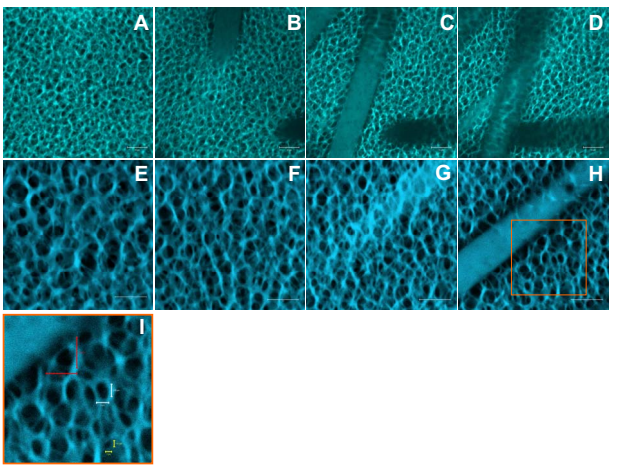

Fig. 5 Optical sections of the confocal and two-photon microscopy of the microporous cellulose membrane with polyester reinforcement fibers. (a) to (d) Confocal micrographs of the Calcofluor-stained membrane at depth=0 (the surface), 10, 20, and 30 μm, respectively. Bar=10 μm. (e) to (h) Two-photon micrographs of the membrane at depth=20, 50, 70, and 80 μm, respectively. Bar=10 μm. (i) An enlarged micrograph of the box shown in (h). Red, white, and yellow bars indicate the pores at the 5-μm, 2-μm, and 1-μm range, respectively. (Color online only.)

2.6 *Postrecording Image Processing and Analysis*

The voxel-based confocal micrographs were processed using the LSM 510 software (Carl Zeiss) and Amira 4.1.2 (Mercury, Chelmsford, Massachusetts) for projection and analysis. In Figs. 3, 4(a)–4(d), 6(a), 7(j), and 7(k), and Videos 1, 2, and 3, the *Voltex* module of Amira was used to project the image stacks and the *Trackball* function was used to adjust the projection angle. In Figs. 5(a)–5(h) and 7(a)–7(i) and Videos 4 and 5, the image stacks were displayed using the *Ortho Slice* function of Amira. The video was made via the *Movie Maker* function of Amira with the increase in display time in association with the depth of the optical section from the surface (beginning) to the interior domain of the construct (end). In Fig. 7(k) and Video 2, the *Volume Editing* function of Amira was used to subtract a cuboid from the scanned volume to expose the interior domain of the sample. In Fig. 6(b), the acquired image stack was displayed using the *Orthogonal Section View* function of the LSM 510 software to present the interior details of the scanned region.

3 Results and Discussion

3.1 *Optical Clearing of Collagen, Chitosan, and Cellulose Scaffolds*

Collagen, chitosan, and cellulose are among the most common natural biomaterials used to fabricate tissue-engineering scaffolds for promoting tissue repair or regeneration. Major advantages of these three biomaterials are their abundance, their proven ability to support the growth/infiltration of a variety of cell types and tissues, and their relatively low immu-

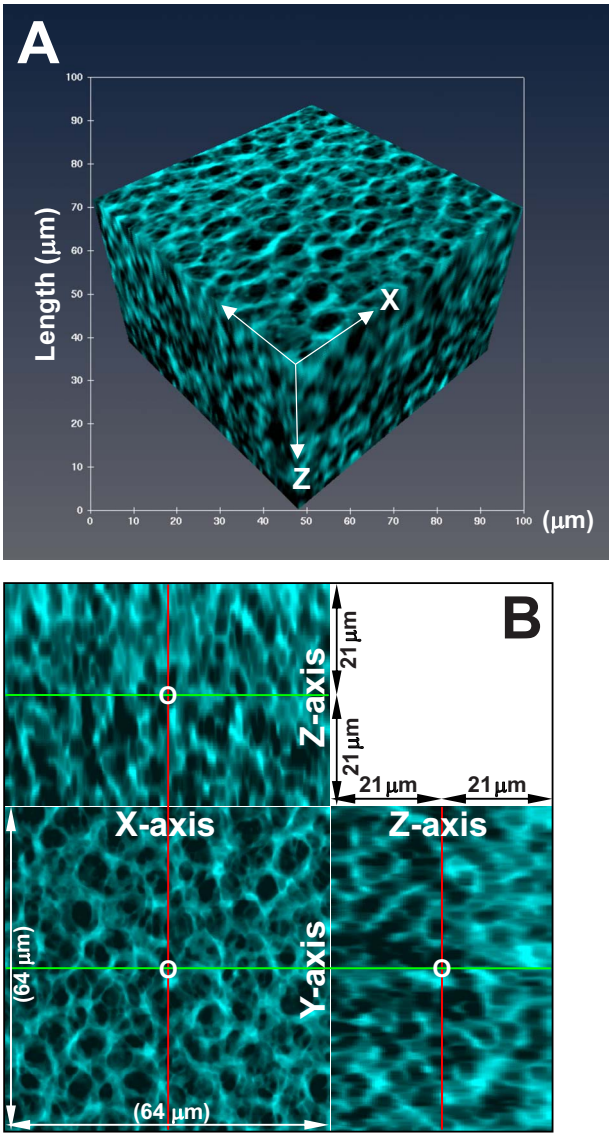

Fig. 6 The exterior and interior details of the scanned 3-D region of the cellulose membrane. (a) Stereo projection of a set of two-photon micrograph stacks showing the exterior of the scanned region with a depth=42 μm and an x/y plane area of 64 μm×64 μm. (b) Orthogonal section views of the image stack to reveal the interior configuration of the imaged membrane segment. The intersection of the three cross sections is indicated by *O*.

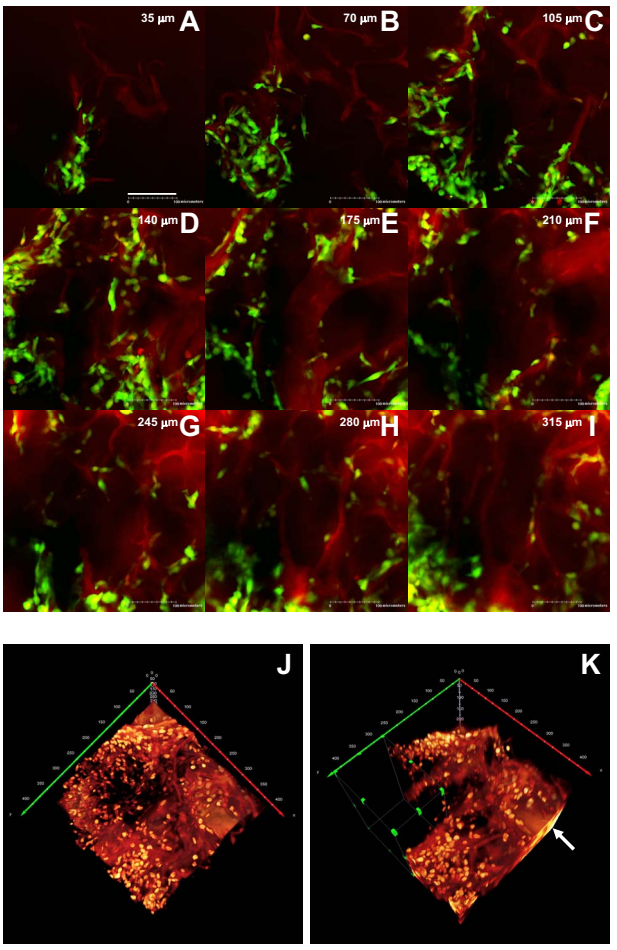

Fig. 7 Penetrative imaging of the fibroblast/collagen construct. (a) to (i) Confocal micrographs at different depths of the fibroblast/collagen construct. The EGFP-labeled human HT-1080 fibroblasts grown in the collagen matrix were stained by propidium iodide (PI) to reveal the nuclei. The PI staining also served as a counterstain to visualize collagen matrices. The serial optical sections from depth=0 to 350 μm are shown in Video 4. Scale bar=100 μm. (j) and (k) Projection of the PI-stained nuclei and collagen matrices using the image stack shown in Video 4 after excluding the EGFP signal. (j): top view; (k): side view. In (k), a cuboid was subtracted from the scanned volume to expose the interior domain of the construct. A 360-deg panoramic presentation of (k) is shown in Video 2. The arrow indicates the lack of image resolution on the x/z plane.

nogenicity. However, scaffolds of collagen, chitosan, and cellulose are intrinsically opaque [Figs. 1(a), 1(b), 1(d), 1(e), 1(g), and 1(h)]. This imposes a barrier to visualize the scaffold architecture in depth and avoids using optical microscopy to *in situ* characterize cellular behavior such as proliferation or differentiation in a 3-D environment. Traditionally, thick collagen, chitosan, and cellulose scaffolds as well as other biological/nonbiological samples are sectioned into thin slices (typically less than 10 μm per slice) to expose their interior domain for microscopic examination. However, the spatial information of the scaffold and tissue structure is often interrupted and/or lost during the sectioning process.

Previously, we have applied an optical-clearing solution, FocusClear, to increase the transparency of insect brains for mapping of neural circuits via confocal microscopy.[22–25] We found that a similar clearing effect was observed when the FocusClear solution was applied to the collagen, chitosan, and cellulose scaffolds [Figs. 1(c), 1(f), and 1(i)]; the thicknesses of the collagen, chitosan, and cellulose matrices were ~3 mm, 1.5 mm, and 250 μm, respectively. In particular, Fig. 1(i) shows that when the cellulose membrane was immersed in the FocusClear solution, the cellulose matrix became transparent, leading to a clear visualization of the polyester reinforcement fibers in the membrane.

3.2 *Quantification of the Optical-Clearing Effect and Its Influence on Fluorescence Detection*

Tissues such as human and animal skin have been used to determine the optical-clearing effect of chemical reagents.[9–12]

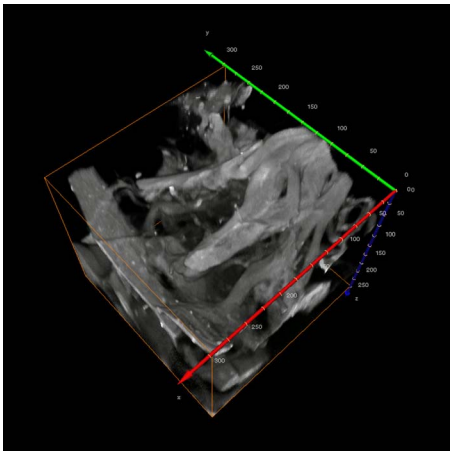

Video 1. A 360-degree panoramic presentation of the collagen scaffold (MPEG, 4.5 MB). [URL: http://dx.doi.org/10.1117/1.3158998.1]

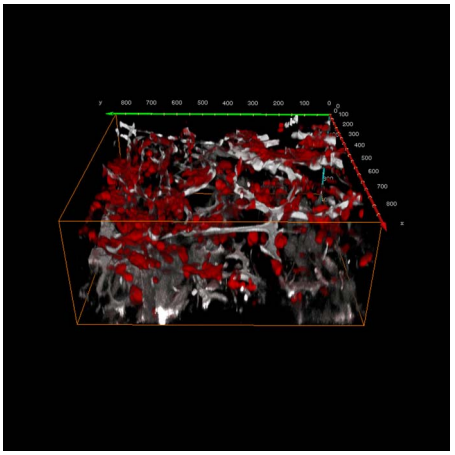

Video 3. A 360-degree panoramic presentation of the osteoblast/chitosan construct (MPEG, 4.9 MB). [URL: http://dx.doi.org/10.1117/1.3158998.3]

However, biological tissues are heterogeneous; they cannot be consistently labeled with fluorescent probes to study the influence of optical clearing on fluorescent signal detection. Alternatively, to quantify the optical-clearing effect, we used aggregates of bovine serum albumin (BSA, heat-induced gel formation,[29,30] ~1,560 μm thick in this experiment) as a light-scattering medium and applied spectrophotometry to measure the transmittance of light across the protein layer [Fig. 2(a)]. Using this method, we compared the efficiency of optical clearing among different immersion solutions. Figure 2(b) shows apart of a 96-well plate with the BSA protein layers immersed in saline (control), FocusClear, and the common optical-clearing reagents DMSO and glycerol. Significantly, after 4-h incubation, one can readily observe that wells with FocusClear were more transparent than those with DMSO or glycerol.

We quantify the optical-clearing effect by measuring the percent transmittance of light across the scattering protein layer. Five wavelengths, 351, 364, 488, 543, and 633 nm (common wavelengths of laser lines for confocal microscopy), were tested. Specifically, Fig. 2(c) shows that at 488 nm, the FocusClear immersion promoted percent transmittance to 48.18% from 1.04% of the saline immersion (control), or by 46.3-fold; a similar increase in transmittance was also observed at 543 and 633 nm. In addition, FocusClear was significantly better than DMSO and glycerol in achieving higher percent transmittance at 488, 543, and 633 nm in the visible light spectrum.

On the other hand, Fig. 2(c) also indicates that ultraviolet (UV) light at 351 and 364 nm suffered low-percent transmittance regardless of the reagent for immersion. It has been known that UV excitation has limited transmissivity in biological tissues due to Rayleigh scattering.[34] Our result indicates that UV radiation at 351 and 364 nm remained strongly scattered by the BSA protein layer despite the FocusClear, DMSO, or glycerol immersion.

To evaluate the impact of optical clearing on fluorescence detection, we next used the 488-nm laser to excite fluorescent probes FITC and EGFP (they were dissolved in the light-scattering BSA medium) and measured the increase in fluorescence emission 200 μm into the BSA gel surface after the

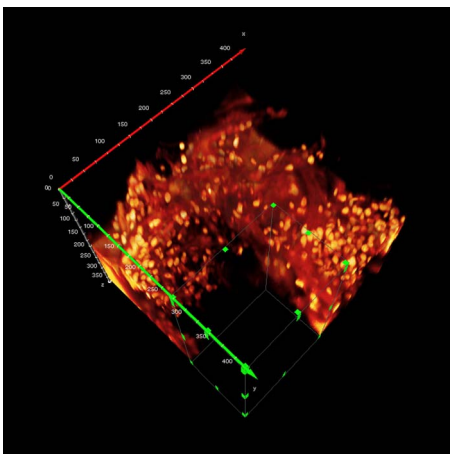

Video 2. A 360-degree panoramic presentation of the volume-edited fibroblast/collagen construct shown in Figure 4(k) (MPEG, 4 MB). [URL: http://dx.doi.org/10.1117/1.3158998.2]

Video 4. Serial confocal micrographs from the surface to depth =350 μm of the fibroblast/collagen construct (MPEG, 4.8 MB). [URL: http://dx.doi.org/10.1117/1.3158998.4]

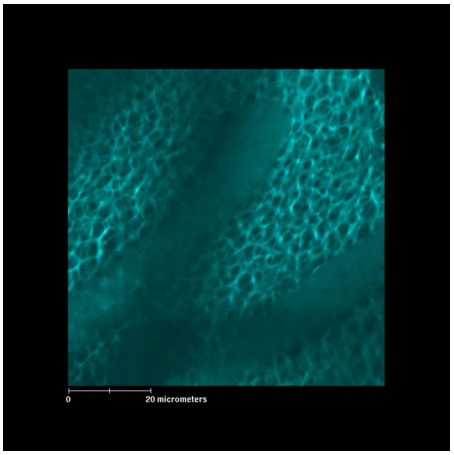

Video 5. Serial confocal micrographs from the surface to depth =40 μm of the microporous cellulose matrix (MPEG, 4.4 MB).
[URL: http://dx.doi.org/10.1117/1.3158998.5]

optical-clearing treatment. Figure 2(d) shows that the FocusClear immersion exhibited 17.2-fold and 6.8-fold increase in fluorescence emission from FITC and EGFP, respectively, in comparison to the saline immersion. Although glycerol and the DAKO aqueous mounting medium also improved fluorescence excitation/emission from the labeled BSA layer; the increase was less significant as compared with that of the FocusClear-mediated optical clearing.

3.3 *Three-Dimensional Imaging of the Collagen Scaffold*

Taking advantage of the transparent collagen scaffold in FocusClear [Fig. 1(c)], we applied confocal microscopy to generate sharp 2-D fluorescence micrographs within the scaffold. Image stacks ranging from depth=0 to 250 μm (101 optical slices, 2.5 μm per increment) were recorded. These digital, voxel-based confocal micrographs were processed using the 3-D *Voltex* projection module of the Amira software to generate a 360-deg panorama of the scanned region (Fig. 3 and Video 1). It is noteworthy that these confocal micrographs were acquired via detection of collagen's autofluorescence induced by the 488-nm argon laser.[31] The result highlights the effectiveness of the FocusClear-mediated optical clearing, which minimized light scattering and allowed confocal microscopy for detection of the low-intensity autofluorescence from the collagen scaffold.

3.4 *Penetrative Imaging of the Fibroblast/Collagen Construct*

We integrated optical clearing and confocal microscopy to visualize cell proliferation/infiltration in the collagen scaffold. Figures 7(a)–7(i) are examples of confocal micrographs at different depths of the fibroblast/collagen scaffold 7 days after cell seeding. These images show the supportive role of collagen fibers for adhesion and proliferation of fibroblasts in the construct. A video file of serial optical sections from the construct surface to depth=350 μm is shown in Video 4. Compared with the microtome-based image acquisition of a thick tissue, optical sectioning microscopy is noninvasive and capable of providing a continuous flow of image information to examine *in situ* a region of the tissue construct.

Figures 7(j) and 7(k) are projections of confocal micrographs that reveal the propidium iodide (PI)–stained nuclei and collagen fibers. Specifically, to expose the interior domain, we used the volume-editing function of the Amira software to subtract a cuboid from the scanned region [Fig. 7(k)]. Video 2 is a 360-deg panoramic presentation of the volume-edited construct. Noticeably, the image resolution of the x/z plane in Fig. 7(k) (indicated by the arrow) and the x/z and y/z planes in Video 2 is lower than that of the x/y plane. The lack of z axis resolution is an inherent limitation of the current optical and mechanical designs of confocal microscopy.

3.5 *Three-Dimensional Imaging of the Chitosan Scaffold*

In addition to the protein scaffold formed by collagen matrices, we also applied confocal microscopy to examine the transparent chitosan scaffold [Fig. 1(f)] Figures 4(a) and 4(b) are 3-D projections of the confocal image stack showing the scanned chitosan scaffold from depth=0 (surface) to 300 μm. The image stack was obtained by detecting the autofluorescence induced by the 488-nm argon laser,[32] similar to what we had used in imaging the collagen scaffold. Significantly, for both the collagen and the chitosan scaffolds, their low-intensity autofluorescence was sufficient to allow in-depth structure visualization- [Figs. 4(a) and 4(b)], underlining the sensitivity of confocal microscopy when integrated with the FocusClear-mediated optical clearing.

3.6 *Penetrative Imaging of the Osteoblast/Chitosan Construct*

Chitosan-based scaffolds have been widely studied in bone tissue engineering for *in vitro* and *in vivo* bone generation. The hydrophilic chitosan scaffolds allow the initial attachment and spreading of osteoblasts,[2] serving as a physical support to guide the growth of new bone tissues. To image the osteoblast/chitosan construct, we applied the penetrative confocal microscopy to visualize the adhesion and infiltration of human Saos-2 osteoblasts after they were seeded on the scaffold for 7 days. Figures 4(c) and 4(d) and Video 3 are projections of the confocal image stack showing that the osteoblasts attached to the chitosan scaffold and followed the scaffold structure in spreading. Unlike the conventional 2-D image analysis showing the infiltration only from a specific cut plane, Video 3 provides a 360-deg panoramic presentation of the scanned region. Specifically, we observed a few osteoblasts infiltrated into the scaffold at depth ~250 μm 7 days post-seeding.

3.7 *Confocal Microscopy of the Internal Matrix Structure of Microporous Cellulose Membranes*

We next applied the penetrative imaging method to characterize cellulose scaffolds in the format of microporous membranes. A few studies have used confocal microscopy to examine the cellulose membrane structure.[35,36] Unfortunately, due to lack of dye labeling (cellulose has a much lower autofluorescence background than collagen or chitosan) and op-

tical clearing of the membrane, the acquired micrographs have poor resolution and cannot clearly present the microporous structure of the cellulose matrix.

We combined Calcofluor (a cellulose-binding UV dye)[33] staining and FocusClear-mediated optical clearing [Fig. 1(i)] to improve the image resolution of confocal microscopy of cellulose matrices. Figures 5(a)–5(d) are examples of confocal micrographs revealing the detailed cellulose membrane structure at the depth=0 (the surface), 10, 20, and 30 μm, respectively. The micrograph stack from z axis=0 to 40 μm are presented in Video 5. It is noteworthy that the image resolution started to decline when the depth was close to 40 μm. The limitation is most likely caused by poor transmission of UV laser through the cellulose sample, thus leading to insufficient Calcofluor excitation.

3.8 *Two-Photon Optical Imaging Improves the Penetration Depth of Imagine the Cellulose Matrix*

We next sought to improve the penetration depth using two-photon optical imaging with the long-wavelength 820-nm Ti-Sapphire infrared laser to excite Calcofluor. In two-photon microscopy, excitation of fluorochrome is achieved by employing high photon density and flux to induce the absorption of two (or multiple) low-energy, infrared photons simultaneously, thus raising the fluorochrome into the excited state for the subsequent fluorescence emission.[37] Infrared radiations are scattered to a lesser degree than those of shorter wavelengths, therefore allowing deeper sample penetration, which is a benefit to high-resolution imaging.

Figures 5(e)–5(h) show the detailed cellulose membrane structure at the depth (z axis)=20 μm, 50 μm, 70 μm, and 80 μm, respectively. Significantly, use of the infrared laser-coupled two-photon microscopy increased the penetration depth to 80 μm from 40 μm of the UV laser-based confocal microscopy, or by 100%. Specifically, Fig. 7(i) shows that pores at the 1-μm range can be identified at z axis=80 μm.

To present the exterior and interior details of the scanned 3-D region, the two-photon optical micrographs were further processed using the 3-D *Voltex* projection module offered by the Amira software [Fig. 6(a)] and the *orthogonal section view* function offered by the LSM 510 software [Fig. 6(b)]. Both Figs. 6(a) and 6(b) were derived from the same two-photon optical image stack with a depth=42 μm and an x/y plane area of 64 μm$\times$64 μm. It is noticeable that similar to confocal microscopy, two-photon optical imaging also suffers lower image resolution at the x/z and y/z planes than at the x/y plane. Nonetheless, despite the obvious need to improve the z-axis resolution of the current optical sectioning microscopy, our new approach of combining optical clearing, confocal/two-photon imaging, and postrecording image processing and projection has extended the view of microscopic tissue scaffolds from planar images to an integrated 3-D presentation.

4 Conclusions

Collagen, chitosan, and cellulose are among the most abundant natural polymers for biomedical and biomaterial applications. Unfortunately, the intrinsic turbidity of scaffolds formed by these three polymers has hindered the utility of optical sectioning microscopy for in-depth scaffold imaging. To overcome this hurdle, we used FocusClear-mediated optical clearing to improve photon penetration, which allowed efficient fluorescence excitation and emission for imaging. We demonstrate that the integration of optical clearing, confocal/two-photon microscopy, and 3-D image rendering provides a useful approach to microscopically examine the scaffold structure. This approach would be a valuable tool to study biomaterials and their interactions with the molecule/cell of interest within the scaffold in an integrated fashion.

Acknowledgments

This work was supported in part by grants from the National Science Council, Taiwan (NSC 96-3112-B-007-005 and NSC 97-2221-E-007-041-MY2) and the Research Development Program, National Tsing Hua University, Taiwan. We thank Dr. Ann-Shyn Chiang and Dr. Hsiu-Ming Chang at NTHU for supporting the imaging techniques.

References

1. S. F. Badylak, "The extracellular matrix as a biologic scaffold material," *Biomaterials* **28**(25), 3587–3593 (2007).
2. A. Di Martino, M. Sittinger, and M. V. Risbud, "Chitosan: a versatile biopolymer for orthopaedic tissue-engineering," *Biomaterials* **26**(30), 5983–5990 (2005).
3. W. Czaja, A. Krystynowicz, S. Bielecki, and R. M. Brown Jr., "Microbial cellulose—the natural power to heal wounds," *Biomaterials* **27**(2), 145–151 (2006).
4. T. J. Sill and H. A. von Recum, "Electrospinning: applications in drug delivery and tissue engineering," *Biomaterials* **29**(13), 1989–2006 (2008).
5. J. D. Schiffman and C. L. Schauer, "One-step electrospinning of cross-linked chitosan fibers," *Biomacromolecules* **8**(9), 2665–2667 (2007).
6. R. van Reis and A. Zydney, "Bioprocess membrane technology," *J. Membr. Sci.* **297**(1–2), 16–50 (2007).
7. J. A. Conchello and J. W. Lichtman, "Optical sectioning microscopy," *Nat. Methods* **2**(12), 920–931 (2005).
8. G. Vogel, "Developmental biology. Lights!Camera! Action! Zebrafish embryos caught on film," *Science* **322**(5899), 176 (2008).
9. R. K. K. Wang, X. Q. Xu, V. V. Tuchin, and J. B. Elder, "Concurrent enhancement of imaging depth and contrast for optical coherence tomography by hyperosmotic agents," *J. Opt. Soc. Am. B* **18**(7), 948–953 (2001).
10. J. Jiang, M. Boese, P. Turner, and R. K. Wang, "Penetration kinetics of dimethyl sulphoxide and glycerol in dynamic optical clearing of porcine skin tissue *in vitro* studied by Fourier transform infrared spectroscopic imaging," *J. Biomed. Opt.* **13**(2), 021105 (2008).
11. E. A. Genina, A. N. Bashkatov, A. A. Korobko, E. A. Zubkova, V. V. Tuchin, I. Yaroslavsky, and G. B. Altshuler, "Optical clearing of human skin: comparative study of permeability and dehydration of intact and photothermally perforated skin," *J. Biomed. Opt.* **13**(2), 021102 (2008).
12. Z. Mao, D. Zhu, Y. Hu, X. Wen, and Z. Han, "Influence of alcohols on the optical clearing effect of skin *in vitro*," *J. Biomed. Opt.* **13**(2), 021104 (2008).
13. M. G. Ghosn, E. F. Carbajal, N. A. Befrui, V. V. Tuchin, and K. V. Larin, "Differential permeability rate and percent clearing of glucose in different regions in rabbit sclera," *J. Biomed. Opt.* **13**(2), 021110 (2008).
14. G. Vargas, J. K. Barton, and A. J. Welch, "Use of hyperosmotic chemical agent to improve the laser treatment of cutaneous vascular lesions," *J. Biomed. Opt.* **13**(2), 021114 (2008).
15. K. Moulton, F. Lovell, E. Williams, P. Ryan, D. C. Lay, D. Jansen, and S. Willard, "Use of glycerol as an optical clearing agent for enhancing photonic transference and detection of *Salmonella typhimurium* through porcine skin," *J. Biomed. Opt.* **11**(5), 054027 (2006).
16. A. T. Yeh and J. Hirshburg, "Molecular interactions of exogenous chemical agents with collagen—implications for tissue optical clear-

ing," *J. Biomed. Opt.* **11**(1), 014003 (2006).
17. M. V. Schulmerich, J. H. Cole, K. A. Dooley, M. D. Morris, J. M. Kreider, and S. A. Goldstein, "Optical clearing in transcutaneous Raman spectroscopy of murine cortical bone tissue," *J. Biomed. Opt.* **13**(2), 021108 (2008).
18. R. LaComb, O. Nadiarnykh, S. Carey, and P. J. Campagnola, "Quantitative second harmonic generation imaging and modeling of the optical clearing mechanism in striated muscle and tendon," *J. Biomed. Opt.* **13**(2), 021109 (2008).
19. H. S. Sakhalkar, M. Dewhirst, T. Oliver, Y. Cao, and M. Oldham, "Functional imaging in bulk tissue specimens using optical emission tomography: fluorescence preservation during optical clearing," *Phys. Med. Biol.* **52**(8), 2035–2054 (2007).
20. M. Oldham, H. Sakhalkar, Y. M. Wang, P. Guo, T. Oliver, R. Bentley, Z. Vujaskovic, and M. Dewhirst, "Three-dimensional imaging of whole rodent organs using optical computed and emission tomography," *J. Biomed. Opt.* **12**(1), 014009 (2007).
21. M. Oldham, H. Sakhalkar, T. Oliver, G. A. Johnson, and M. Dewhirst, "Optical clearing of unsectioned specimens for three-dimensional imaging via optical transmission and emission tomography," *J. Biomed. Opt.* **13**(2), 021113 (2008).
22. Y. L. Wang, A. Mamiya, A. S. Chiang, and Y. Zhong, "Imaging of an early memory trace in the *Drosophila* mushroom body," *J. Neurosci.* **28**(17), 4368–4376 (2008).
23. H. H. Lin, J. S. Lai, A. L. Chin, Y. C. Chen, and A. S. Chiang, "A map of olfactory representation in the *Drosophila* mushroom body," *Cell* **128**(6), 1205–1217 (2007).
24. C. L. Wu, S. Xia, T. F. Fu, H. Wang, Y. H. Chen, D. Leong, A. S. Chiang, and T. Tully, "Specific requirement of NMDA receptors for long-term memory consolidation in *Drosophila* ellipsoid body," *Nat. Neurosci.* **10**(12), 1578–1586 (2007).
25. Y. C. Liu and A. S. Chiang, "High-resolution confocal imaging and three-dimensional rendering," *Methods* **30**(1), 86–93 (2003).
26. Y. L. Chen, H. P. Lee, H. Y. Chan, L. Y. Sung, H. C. Chen, and Y. C. Hu, "Composite chondroitin-6-sulfate/dermatan sulfate/chitosan scaffolds for cartilage tissue engineering," *Biomaterials* **28**(14), 2294–2305 (2007).
27. Z. H. Wang, W. C. Chien, T. W. Yue, and S. C. Tang, "Application of heparinized cellulose affinity membranes in recombinant adeno-associated virus serotype 2 binding and delivery," *J. Membr. Sci.* **310**(1–2), 141–148 (2008).
28. S. J. Tseng and S. C. Tang, "Development of poly (amino ester glycol urethane)/siRNA polyplexes for gene silencing," *Bioconjugate Chem.* **18**(5), 1383–1390 (2007).
29. M. Murata, F. Tani, T. Higasa, N. Kitabatake, and E. Doi, "Heat-induced transparent gel formation of bovine serum-albumin," *Biosci., Biotechnol., Biochem.* **57**(1), 43–46 (1993).
30. C. Veerman, L. M. C. Sagis, J. Heck, and E. van der Linden, "Mesostructure of fibrillar bovine serum albumin gels," *Int. J. Biol. Macromol.* **31**(4–5), 139–146 (2003).
31. D. S. Gareau, P. R. Bargo, W. A. Horton, and S. L. Jacques, "Confocal fluorescence spectroscopy of subcutaneous cartilage expressing green fluorescent protein versus cutaneous collagen autofluorescence," *J. Biomed. Opt.* **9**(2), 254–258 (2004).
32. C. Cunha-Reis, K. TuzlaKoglu, E. Baas, Y. Yang, A. El Haj, and R. L. Reis, "Influence of porosity and fiber diameter on the degradation of chitosan fiber mesh scaffolds and cell adhesion," *J. Mater. Sci.: Mater. Med.* **18**(2), 195–200 (2007).
33. B. J. Harrington and G. J. Hageage, "Calcofluor white: a review of its uses and applications in clinical mycology and parasitology," *Lab Med.* **34**(5), 361–367 (2003).
34. J. W. Lichtman and J. A. Conchello, "Fluorescence microscopy," *Nat. Methods* **2**(12), 910–919 (2005).
35. S. R. Wickramasinghe, J. O. Carlson, C. Teske, J. Hubbuch, and M. Ulbricht, "Characterizing solute binding to macroporous ion exchange membrane adsorbers using confocal laser scanning microscopy," *J. Membr. Sci.* **281**(1–2), 609–618 (2006).
36. M. Ferrando, A. Rozek, M. Zator, F. Lopez, and C. Guell, "An approach to membrane fouling characterization by confocal scanning laser microscopy," *J. Membr. Sci.* **250**(1–2), 283–293 (2005).
37. F. Helmchen and W. Denk, "Deep tissue two-photon microscopy," *Nat. Methods* **2**(12), 932–940 (2005).